CLIMATOLOGY

Enhanced Atlantic Meridional Mode predictability in a high-resolution prediction system

Qiuying Zhang^{1*}, Ping Chang^{1,2}, Dan Fu¹, Stephen G. Yeager³, Gokhan Danabasoglu³, Frederic Castruccio³, Nan Rosenbloom³

Accurate prediction of sea surface temperatures (SSTs) in the tropical North Atlantic on multiyear timescales is of paramount importance due to its notable impact on tropical cyclone activity. Recent advances in high-resolution climate predictions have demonstrated substantial improvements in the skill of multiyear SST prediction. This study reveals a notable enhancement in high-resolution tropical North Atlantic SST prediction that stems from a more realistic representation of the Atlantic Meridional Mode and the associated wind-evaporation-SST feedback. The key to this improvement lies in the enhanced surface wind response to changes in cross-equatorial SST gradients, resulting from Intertropical Convergence Zone bias reduction when atmospheric model resolution is increased, which, in turn, amplifies the positive feedback between latent and sensible surface heat fluxes and SST anomalies. These advances in high-resolution climate prediction hold promise for extending tropical cyclone forecasts at multiyear timescales.

Copyright © 2024 The Authors, some rights reserved; exclusive licensee American Association for the Advancement of Science. No claim to original U.S.
Government Works.
Distributed under a Creative Commons Attribution
NonCommercial
License 4.0 (CC BY-NC).

INTRODUCTION

Sea surface temperature (SST) variability in the tropical North Atlantic (TNA) plays a crucial role in various important weather and climate hazards, most notably seasonal tropical cyclone (TC) activity. In particular, the main development region (MDR; see Fig. 1A) within TNA serves as a vital area where many TCs form and intensify (1–3). Thus, enhancing the predictive capacity for MDR SST is a critical prerequisite for developing a reliable TC prediction system at climate timescales. However, the intricate and multifaceted mechanisms governing SST evolution in MDR pose a substantial challenge to improve SST prediction skill.

Observational analyses have demonstrated that MDR SSTs are strongly influenced by the Atlantic Meridional Mode (AMM), which is characterized by a cross-equatorial gradient of SST anomaly (SSTA) and wind anomalies that traverse the equator, varying on multiyear timescales (4–7). A positive AMM features positive SSTA in TNA accompanied by a C-shaped northward cross-equatorial wind anomaly (5, 6, 8).

Previous studies have proposed that the emergence of AMM may be attributed to both remote influences and a local thermodynamic air-sea coupling mechanism known as wind-evaporation-SST (WES) feedback (5, 9). Remote influences include factors such as the El Niño–Southern Oscillation (ENSO), the North Atlantic Oscillation (NAO), and subpolar North Atlantic (SPNA) SST variability (10–14). In contrast, the WES feedback in the tropical Atlantic involves the interplay between cross-equatorial wind anomalies, wind-induced turbulent heat fluxes, and SST (4, 5, 15). AMM accounts for ~66% of the monthly SST variance in the tropical Atlantic coupled system after removing ENSO influences (4) and, thus, can potentially contribute substantially to tropical Atlantic SST predictability. Because the WES feedback is directly linked to the interaction between cross-equatorial SST gradient and wind anomalies, it

is highly sensitive to the location of the Intertropical Convergence Zone (ITCZ) (12). The seasonal migration of the ITCZ contributes to a strong seasonality of the WES feedback. This feedback develops during boreal winter, reaches its peak in boreal spring when the ITCZ moves closest to the equator, and gradually weakens as the ITCZ shifts northward.

While simulated AMM in models participating in the Coupled Model Intercomparison Projects (CMIPs) shows a similar spatial pattern to observations, its development appears highly unrealistic. In these models, wind anomalies during boreal winter are exaggerated, but their response to SST anomalies in the subsequent spring is much weaker than observed, indicating a flawed representation of AMM genesis (4). This modeling issue, potentially linked to an underestimated coupling strength between the atmosphere and ocean, may compromise SST prediction skill in TNA. However, a recent study comparing low- and high-resolution climate prediction systems based on the Community Earth System Model version 1 (CESM1) shows that increased resolution notably improves SST prediction skill over multiyear timescales (16). The present study aims to uncover the reasons behind the enhanced SST prediction skill in TNA within the high-resolution CESM1.

The CESM1 high-resolution decadal prediction system (HRDP) (16) has a finer horizontal resolution (0.25° for atmosphere and land and 0.1° for ocean and sea ice) than the CESM1 decadal prediction large ensemble (DPLE) (17), which uses a standard low horizontal resolution (1°). Both use similar initialization procedures based primarily on forced ocean sea-ice simulations (FOSIs) with consistent respective resolutions, using observation-based atmospheric forcing from the Ocean Model Intercomparison Project (OMIP) (18, 19). For direct comparison, we select predictions initialized on the same dates, every other 1 November from 1976 to 2016, totaling 21 ensembles. Each HRDP ensemble comprises 10-member 5-year prediction runs, while DPLE has 40-member 10-year prediction runs. To analyze the resolution sensitivity of intrinsic AMM and WES feedbacks, we also compare preindustrial simulations (PI) at high resolution (PI-HR) (20) and standard low resolution (PI-LR) (21). Further details are in Materials and Methods.

¹Department of Oceanography, Texas A&M University, College Station, TX, USA. ²Department of Atmospheric Sciences, Texas A&M University, College Station, TX, USA. ³National Science Foundation National Center for Atmospheric Research, Boulder, CO, USA.

^{*}Corresponding author. Email: zhangqiuying@tamu.edu.

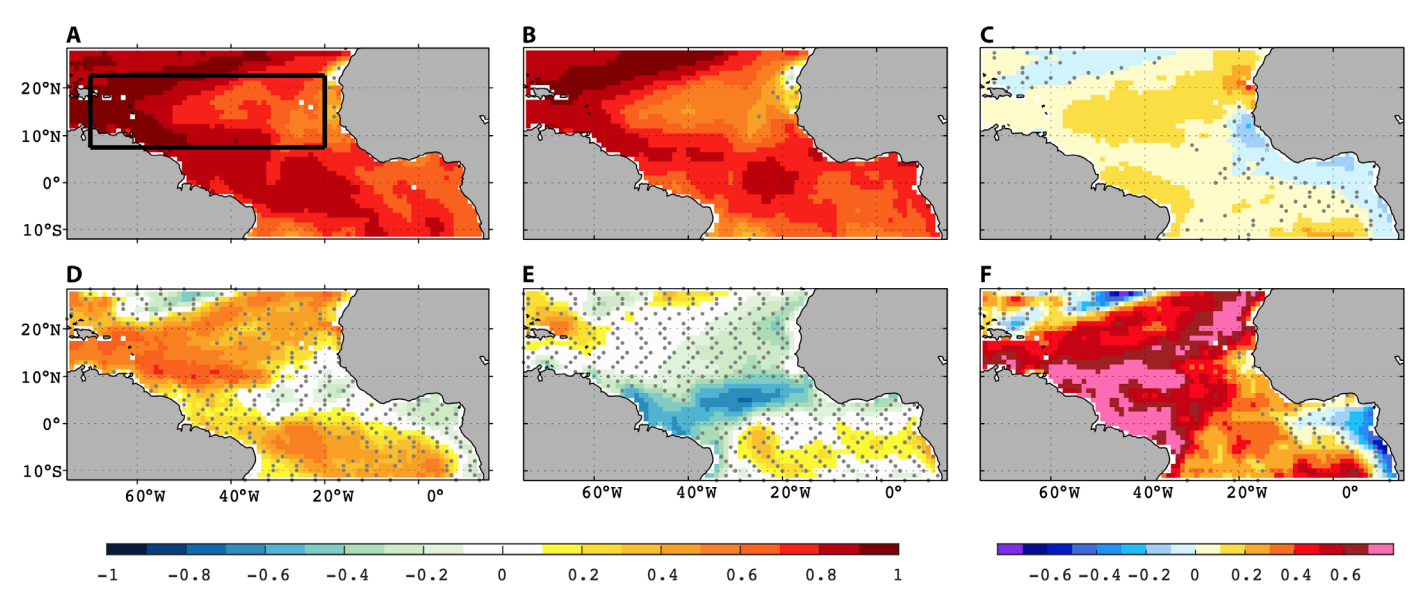


Fig. 1. LY1-5 SST annual prediction skill measured by ACC. ACC scores for (\mathbf{A} and \mathbf{D}) 10-member HRDP, (\mathbf{B} and \mathbf{E}) 10-member DPLE, and (\mathbf{C} and \mathbf{F}) ACC differences (Δ ACC) between HRDP and DPLE for [(\mathbf{A}) to (C)] total and [(D) to (F)] natural variability. All the ACC scores are relative to HadISST. Dots in (\mathbf{A}), (\mathbf{B}), (D), and (E) indicate ACC below 95% significant level, and dots in (C) and (F) indicate that ACC score in HRDP is within the 0.95/0.05 quantile values of bootstrapped 10-member DPLE ACC scores. The black box (70°W to 20°W and 7.5°N to 22.5°N) in (\mathbf{A}) is the MDR.

RESULTS

SST prediction skill at one to five lead years

SST prediction skill, assessed using five–lead year average (LY1-5) anomaly correlation coefficient (ACC) scores (see Materials and Methods), reveals HRDP consistently outperforming DPLE by up to 0.2 in the TNA basin (Fig. 1, A to C). This improvement is substantial, considering that ACC in DPLE is already above 0.8 in many areas and the ACC value cannot exceed one. The enhanced ACC in HRDP shows seasonal variations, with the maximum ACC difference (Δ ACC) in TNA between HRDP and DPLE occurring during boreal spring (fig. S1). This timing coincides with the peak season of AMM and WES feedback (4, 12).

A substantial portion of the high ACC scores can arise from externally forced response (22–25). To remove this forced component and focus on the internal component related directly to the initial ocean states, we subtract the forced change from the predicted and observed SST anomalies (see Materials and Methods) (26–29). The remaining internal component driven by natural climate variability shows even higher relative ACC scores in HRDP compared to DPLE in the TNA, particularly in the MDR, where Δ ACC shows a value approaching 0.8 (Fig. 1F). This suggests that while external forcing dominates the SST predictability in DPLE, a substantial fraction of the predictable SST signal variance in the TNA region is attributable to natural climate variability captured by HRDP.

To identify the dominant mode of natural variability, we conduct an empirical orthogonal function (EOF) analysis on the observed pentadal natural SSTA after regressing out Niño3 and NAO indices that may affect TNA SST variations remotely according to previous studies (11–13). The analysis of the remote impact will be discussed in a later subsection. The first EOF, explaining ~50% of the SST variance, depicts a dipole-like SSTA, and the regressed wind stress anomalies show a northward C-shaped cross-equatorial flow. This pattern represents the well-known characteristics of AMM (Fig. 2A) (6). We then regressed LY1-5 predicted SSTA and wind stress anomalies onto the

first observed principal component (PC) of SST and assessed the degree to which the predicted SSTA and wind stress anomaly pattern (Fig. 2, B and C) can replicate the observed AMM (Fig. 2A). The results show that HRDP captures the observed AMM pattern more realistically than DPLE, with a pattern correlation of over 0.4 for TNA SSTAs compared to ~0.1 in DPLE. The predicted cross-equatorial flow over the western Atlantic is also much stronger and closer to the observations in HRDP than in DPLE.

To further investigate whether AMM is more realistically captured by HRDP, we conduct a maximum covariance analysis (MCA) on predicted SST and wind stress anomalies at LY1-5, as well as the corresponding observed pentadal fields, after removing the forced response and remote influences from ENSO and NAO (see Materials and Methods). Although the leading MCA modes, which explain 79.9, 73.2, and 78.4% of the squared covariance in observations, HRDP, and DPLE, respectively, depict similar characteristics of AMM, the pattern in HRDP more closely resembles the observations both in terms of strength and structure compared to DPLE (Fig. 3, A to C). In particular, both the magnitudes of SST and wind stress are much weaker in DPLE, and the maximum near-equatorial meridional SST gradient is too diffuse and extends too far southward. These findings provide an initial indication that HRDP is more skillful in predicting AMM due to its increased horizontal resolution. This claim is further validated by regressing the LY1-5 predicted TNA SSTA onto the observed leading MCA SST pattern (Fig. 3A) and correlating the resultant time series with the corresponding time series from the observed MCA. HRDP yields an ensemble mean correlation value of ~0.7, significantly higher than DPLE's value of ~0.5. Thus, these analyses support the notion that HRDP is more skillful in predicting AMM compared to DPLE.

Improved WES feedback by increasing model resolution

We next examine and compare the WES feedback in observations, HRDP, and DPLE because it lies at the heart of AMM dynamics

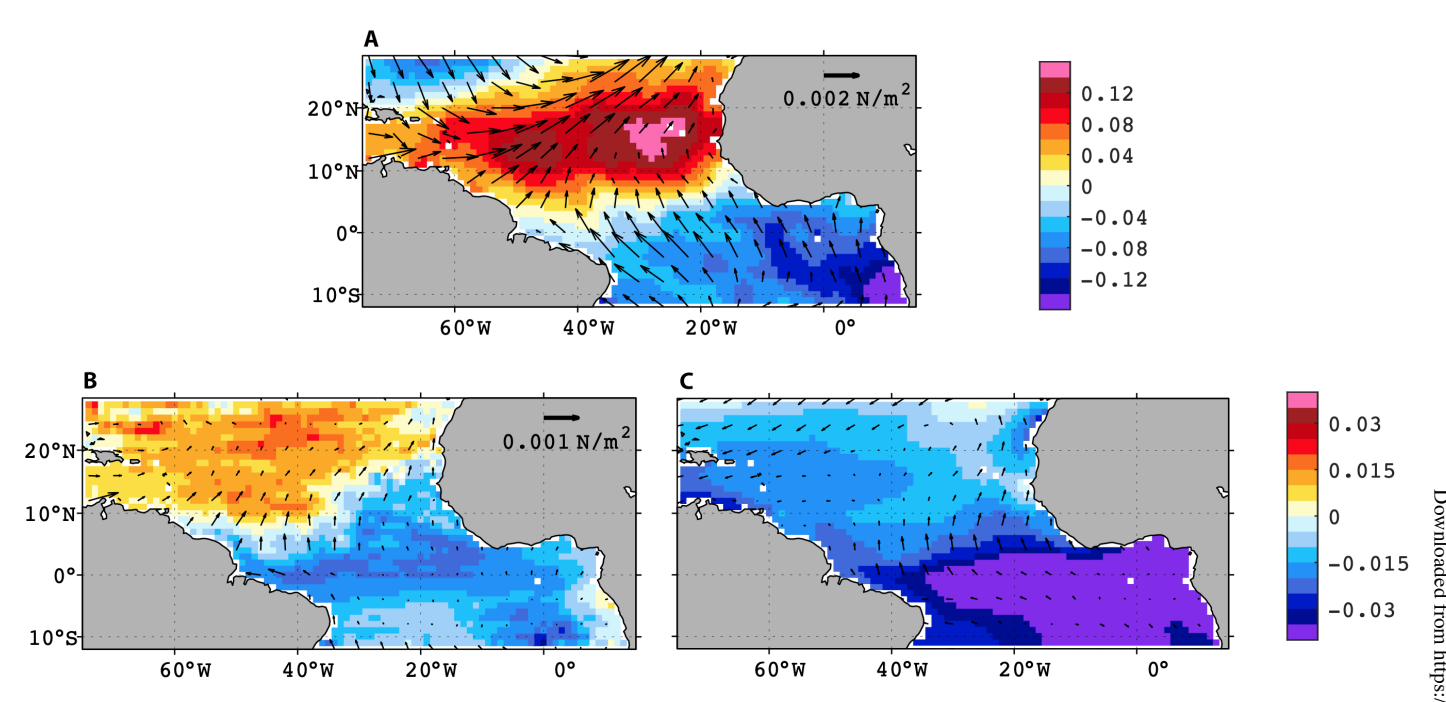


Fig. 2. Predicted AMM pattern at LY1-5. SST (color shading; °C) and wind stress vector (vectors; in newtons per square meter) anomalies regressed on the normalized leading PC of HadlSST in (A) observations, (B) 10-member HRDP, and (C) 10-member DPLE. The EOF analysis of pentadal observed SST is based on the region 75°W to 15°E and 12°S to 28°N. The scale of wind stress vectors in (A) is 0.002 N/m², twice that of (B) and (C).

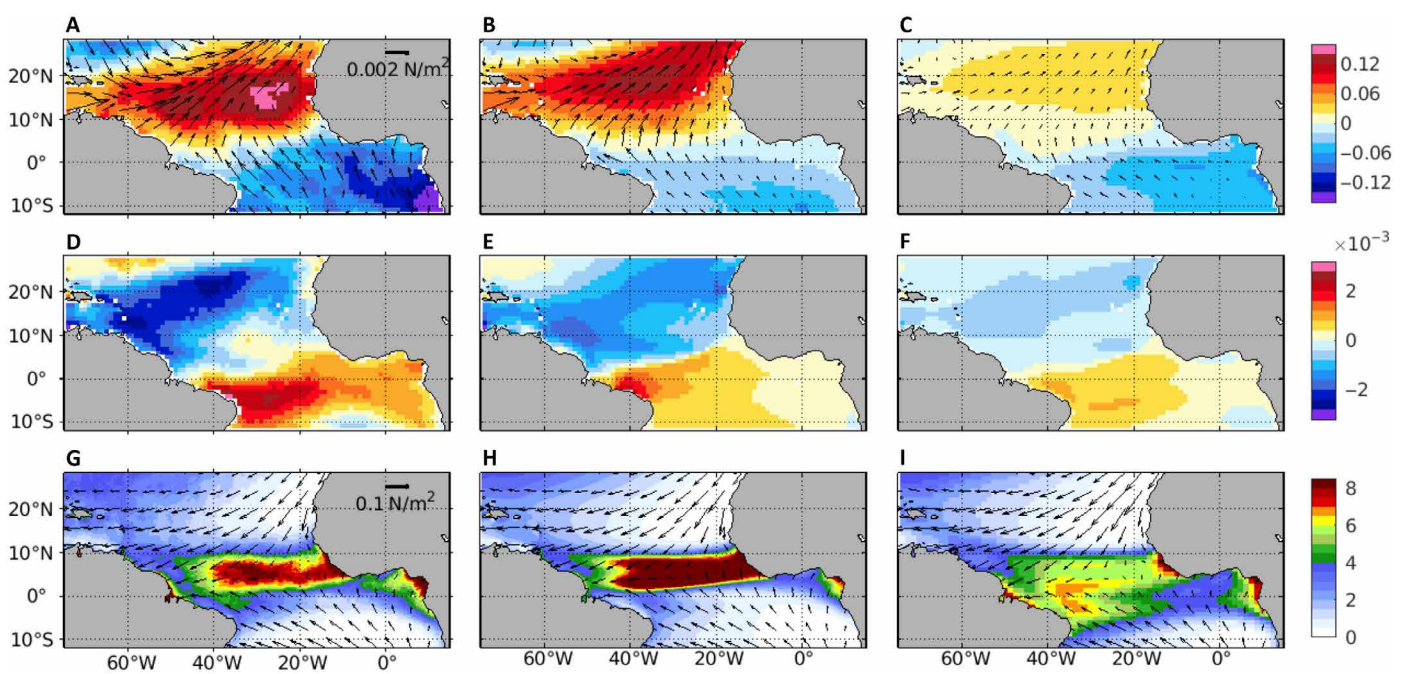


Fig. 3. AMM and annual mean ITCZ at LY1-5. (A to C) The leading MCA mode in SST (color shading; °C) and wind stress vector (vectors; in newtons per square meter) in observations, 10-member HRDP, and 10-member DPLE, respectively. (D to F) WSAAs (in newtons per square meter) regressed onto the normalized expansion coefficient in observations, 10-member HRDP, and 10-member DPLE, respectively. (G to I) Annual mean precipitation (color shading; in millimeters per day) and wind stress vector (vectors; in newtons per square meter) in observations, 10-member HRDP, and 10-member DPLE, respectively. The wind stress vectors in (A) to (C) share the same scale that is shown in (A), and those in (G) to (I) share the same scale that is shown in (G). (B), (C), (E), and (F) are the average of the regressions from individual members.

(5, 27). This is achieved by regressing the observed and predicted LY1-5 wind stress amplitude anomalies (WSAAs) onto the normalized SST expansion coefficient of the leading MCA (Fig. 3, D to F). We opt to use WSAA instead of turbulent heat flux anomalies due to high uncertainties associated with the latter in observations. In the western TNA, a clear relationship between positive SSTA and negative WSAA is observed. This relationship signifies positive feedback between SST and turbulent heat fluxes because the reduced WSAA over the positive SSTA can lead to a reduction in latent and sensible heat release from the ocean, amplifying the positive SSTA. This positive feedback is a fundamental aspect of the WES feedback (5, 27). Although both HRDP and DPLE exhibit weaker WSAA strength compared to observations, only HRDP realistically captures the negative maximum over the western TNA, indicating a more robust and realistic WES feedback in HRDP than DPLE.

Accompanied with the superior performance of WES feedback in HRDP, the predicted position of ITCZ in HRDP aligns more closely with the observation compared to DPLE. In HRDP, the ITCZ is confined between the equator and 10°N from the west coast of Africa, extending to ~40°W, as shown by the climatological annual mean precipitation and wind stress (Fig. 3, G to I). In contrast, DPLE exhibits a broader and weaker double ITCZ. The spatial correlation of precipitation between observation and HRDP over the ocean domain (60°W to 0°) can reach 0.90 in the deep tropics (10°S to 10°N), while it is 0.78 between observation and DPLE. Given the simultaneous improvements in WES and ITCZ, we hypothesize that the improved ITCZ location in HRDP plays an important role in the enhanced prediction skill of AMM through improving WES feedback. We will delve deeper into this hypothesis in the subsequent section.

Because AMM and WES are intrinsic to the coupled climate system, the impact of model resolution on the representation of AMM and WES can be assessed using the long PI-HR and PI-LR simulations without the influence of initialization. To align with the record length of the observations, we randomly choose 20 independent 52-year-long monthly samples from PI-HR and PI-LR. MCA analysis is then conducted for each sample, and the sample mean of model leading MCAs is compared to the observed leading MCA. Recognizing amplitude differences, we normalized all MCAs by dividing each by its maximum value for a more effective comparison of pattern differences (see Materials and Methods). Although all the leading MCAs during boreal spring (March to April to May), which is the peak season of WES feedback in TNA, show similar overall patterns, the MCA in PI-HR more closely mirrors the observed pattern than that in PI-LR, particularly in the deep tropics where the crossequatorial SST gradient and C-shaped cross-equatorial wind anomalies in PI-LR are notably weaker, with most variability of SST and wind stress anomalies shifted to the northern TNA (fig. S2, A to F).

Further information about the WES feedback is obtained from analyzing the expansion coefficient of SST and wind stress from MCA. Lead-lag correlation analyses reveal comparable values between PI-HR and observations but notably lower values in PI-LR, suggesting a stronger coupling in the former than in the latter (fig. S2G). Comparing SST and wind stress variances across calendar months indicates that PI-HR captures better the observed variability, highlighting the strong atmospheric variability during boreal winter as the initial driver of TNA SSTA, which is then amplified through the WES feedback in the subsequent spring season (fig. S2, H and I). In contrast, PI-LR exhibits comparable peak winter wind variance but

a delayed peak in SST variance in the summer season, indicating an underestimated SST feedback on the atmosphere (fig. S2J). Combining these findings, we attribute the improved SST prediction skill in TNA in HRDP to the realistic representation of AMM and the associated WES feedback.

Potential factors shaping the WES feedback

To identify factors contributing to the WES feedback disparities between high- and low-resolution simulations, we conduct an AMM event composite (Fig. 4). Again, to facilitate a more effective comparison of pattern differences between simulations and observations, we normalize all the composites by dividing each by its maximum value of the AMM event period (see Materials and Method). In both PI-HR and PI-LR, warm anomalies initially appear in the northeastern TNA during October to November of the preceding AMM year (Oct0 to Nov0), accompanied by the negative WSAA. A notable difference is that in subsequent development, anomalies in PI-LR remain relatively stationary, while in PI-HR, they propagate westward and equatorward, consistent with observations. During February to March (Feb1 to Mar1), PI-HR exhibits pronounced cross-equatorial wind stress anomalies and a stronger SSTA gradient near the equator, contrasting with PI-LR's strong anomalies remaining in the northeastern TNA. As the AMM peaks in April to May (Apr1 to May1), observation and PI-HR both display stronger WSAA negative maximum in the western deep tropics as a part of strong cross-equatorial wind stress anomalies, while PI-LR shows much weaker SST gradient and wind stress anomalies near the equator.

Precipitation anomalies are closely linked to surface wind convergence and divergence anomalies. In PI-HR, a dipole pattern of precipitation anomalies forms during Dec0 to Jan1, peaks in Apr1 to May1, and weakens subsequently, while in PI-LR, a larger-scale dipole precipitation anomaly manifests only during Apr1 to May1 (Fig. 4). These differences in precipitation anomalies are likely linked to the notable differences in the seasonal variations (location and strength) of the precipitation between PI-HR and PI-LR, which can influence the AMM and WES feedback (*12*). It is worth noting the reduction of the notorious double-ITCZ bias in PI-HR, resulting in a more realistic ITCZ compared to PI-LR.

To further ascertain the impact of atmosphere versus ocean resolution, we analyzed two sets of uncoupled simulations. The first set has high-resolution (0.1°) and low-resolution (1°) FOSIs (FOSI-HR and FOSI-LR, respectively; see Materials and Methods), and the second set has high-resolution (0.25°) and low-resolution (1°) atmospheric model intercomparison project style simulations (AMIP-HR and AMIP-LR, respectively; see Materials and Methods). Comparing AMM event composites in FOSI-HR and FOSI-LR reveals similar amplitudes of the simulated meridional SST gradient (Fig. 5, A, E, I, and M) under the same atmospheric forcing (Fig. 5, B, F, J, and N), suggesting a minimal impact of ocean resolution changes. However, in AMIP-HR, a 50% increase in the amplitude of meridional wind stress anomalies compared to AMIP-LR (Fig. 5H), coupled with AMIP-HR more robust precipitation dipole during February to May (Fig. 6), indicates a substantial impact of atmospheric resolution on the strength of WES. These findings underscore the greater impact of increasing atmospheric resolution on enhancing WES feedback, leading to the conclusion that the strengthening of the WES feedback in high-resolution simulations is primarily attributable to the increase in atmospheric resolution, enhancing the near-equatorial atmospheric response to SSTA gradient.

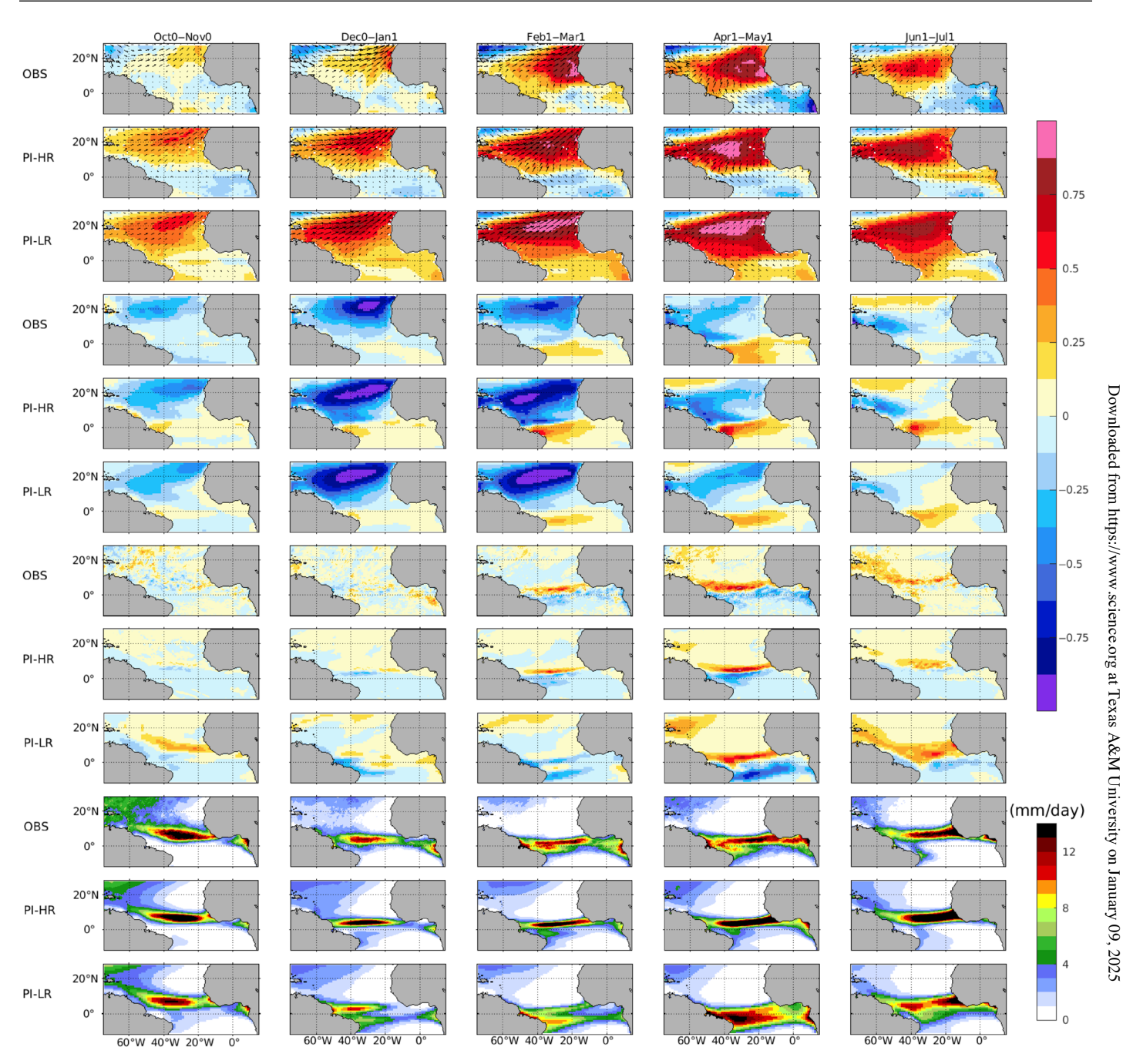


Fig. 4. Development of AMM event composite. (First to third rows) Normalized composite of anomalous SST (color shading) and wind stress vector (vectors) in (row 1) HadlSST/ERA5 (labeled as OBS), (row 2) PI-HR, and (row 3) PI-LR. (Fourth to sixth rows) Normalized composite of WSAA in (row 4) ECMWF Reanalysis v5 (ERA5), (row 5) PI-HR and (row 6) PI-LR. (Seventh to ninth rows) Normalized composite of precipitation anomalies in (row 7) Global Precipitation Measurement (GPM), (row 8) PI-HR, and (row 9) PI-LR. (10th to 12th rows) Precipitation climatologies (in millimeters per day) in (row 10) GPM, (row 11) PI-HR, and (row 12) PI-LR. Each column shows a 2-month average from October before the AMM event year (Oct0) to July (Jul1).

Role of remote impact in SST prediction

While the above analyses emphasize the primary role of AMM and WES feedback in TNA SST prediction, remote impacts also play a role in influencing regional SST dynamics. The impact of remote factors on SST prediction can vary on the basis of the characteristics of a chosen index itself and the regression pattern onto the index. In the following, we examine and compare both these factors between HRDP and DPLE.

Previous studies suggest that modes of variability, such as ENSO, NAO, and SPNA SST, can remotely influence SST variability in TNA. In our analysis, we focus on ENSO and NAO, along with two SST indices in the southeastern Pacific (SEP) and the eastern Pacific Southern Ocean (EPSO), where HRDP has shown significant skill improvement (16). However, we exclude examining the influence from the SPNA SST, as prediction skill in this region degrades in

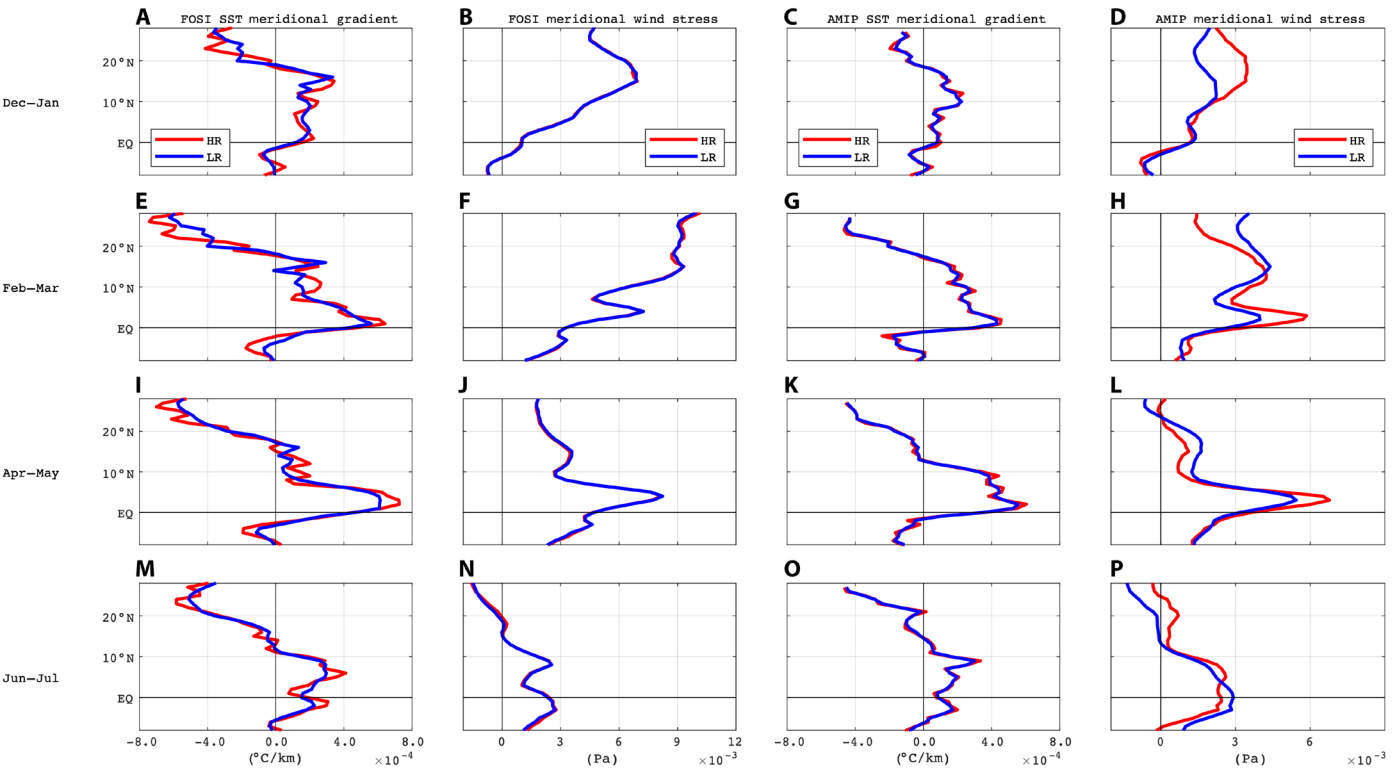


Fig. 5. Evolution composites of anomalous meridional SST gradient and wind stress at AMM event year for uncoupled simulations. Zonal averages between 45°W and 15°W of (first and third columns) meridional SST gradient anomalies from FOSI-HR (red line) and FOSI-LR (blue line) and (second and fourth columns) meridional wind stress anomalies from AMIP-HR (red line) and AMIP-LR (blue line).

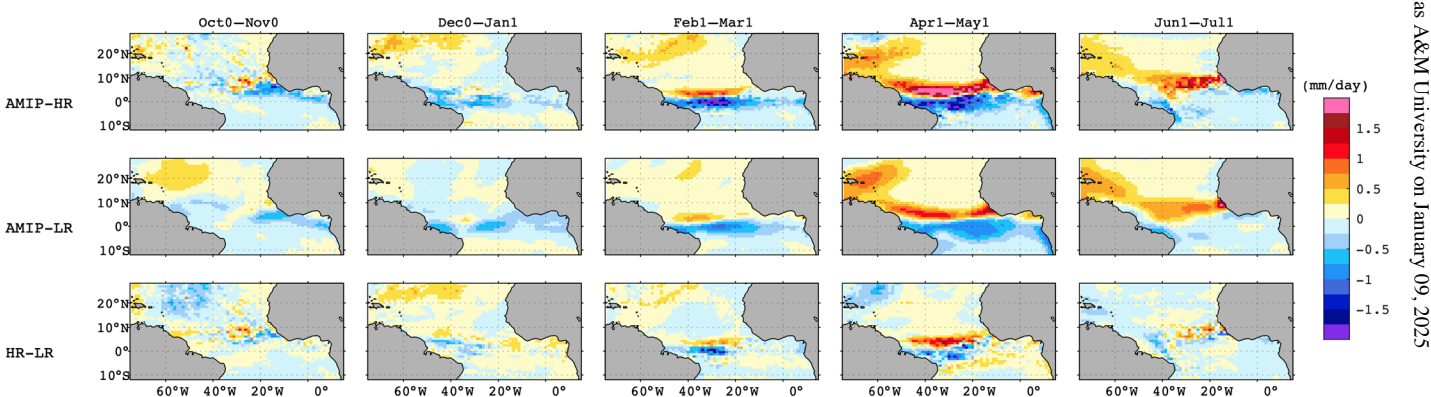


Fig. 6. Precipitation anomalies from AMM event composite for uncoupled AMIP simulations. (Top two rows) Composite of precipitation anomalies (in millimeters per day) in (row 1) AMIP-HR and (row 2) AMIP-LR. (Bottom row) The composite differences of precipitation anomalies between AMIP-HR and AMIP-LR. Each column shows 2-month average from October in the prevous AMM event year (Oct0) to July (Jul1).

HRDP compared to DPLE. The ACC scores of the predicted Niño3, NAO, SEP, and EPSO indices at LY1-5 in HRDP and DPLE are summarized and compared in table S1. A bootstrap analysis with 10 randomly selected ensemble members from 40-member DPLE is used to test whether the difference in ACC scores between HRDP and DPLE is significant.

HRDP generally exhibits higher ACC scores than DPLE for predicting these four indices (table S1), indicating improved prediction skill. However, the improved ACC score for Niño3 in HRDP falls within the SD of the ACC score in DPLE, while the predicted NAO

index at LY1-5 does not pass the significant test in either HRDP (0.21) or DPLE (-0.11). HRDP only demonstrates significant skill improvement for SEP and EPSO, suggesting that remote influences from the South Pacific may contribute to enhanced SST prediction in TNA.

Remote impacts are also influenced by the regression pattern onto these indices (fig. S3). The regression of predicted SSTA at LY1-5 onto each of these four indices reveals that both HRDP and DPLE tend to overestimate the remote impacts from Niño3, SEP, and EPSO at multiyear timescales compared to observations. However,

HRDP, relative to DPLE, exhibits smaller remote impact biases in the deep tropics (between 0° and 10°N) and along the western boundary of the South Tropical Atlantic from Niño3 and SEP (fig. S3, M and O) and in almost the whole North Tropical Atlantic from EPSO (fig. S3P). As a result, HRDP demonstrates improvements in both factors influencing remote impacts over DPLE. These enhancements suggest that remote impacts from Niño3, SEP, and EPSO may also contribute to the improved SST prediction in HRDP.

That said, the enhancements in remote impact are predominantly observed within the deep tropics in HRDP. In contrast, the improved SST prediction extends across a broader area in TNA, particularly along a diagonal from the western deep tropics to the west coast of North Africa (Fig. 1, C and F). In addition, the NAO-related remote impact in HRDP exhibits a larger bias in the TNA compared to DPLE (fig. S3N), despite the higher ACC score of the predicted NAO index. Taking all these factors into account, we conclude that the role of remote impacts in the enhanced SST prediction in HRDP is secondary.

DISCUSSION

The improved prediction skill of AMM-related SST in TNA in HRDP holds notable implications for climate-scale predictability, especially concerning North Atlantic TCs. Given the robust connection between TC activities, ITCZ, and AMM, particularly in the Caribbean (2, 6, 7, 10, 12, 30–32), HRDP, with its ability to explicitly simulate TC-like features, is expected to demonstrate useful skill in predicting TC track density anomalies. This expectation holds true at LY1, where the ACC between observed and HRDP-predicted TC track density during the TC season (June to November) reveals high values in the western TNA region centered around the Caribbean Sea, with peak scores approaching 0.7 (Fig. 7A). These high skill scores align with the high ACC values of the corresponding SSTA in the same region (Fig. 7B), affirming the substantial impact of local SST conditions on TC activity.

However, the analysis of ACC for TC track density anomalies reveals a rapid deterioration in skill scores beyond LY1 (fig. S4), indicating HRDP struggles to maintain its high skill beyond 1 year. A potential contributor to this declining skill at longer lead times is HRDP's cold SST bias in TNA, which escalates notably with increasing lead time (fig. S5). At LY1, the predicted climatological mean SST in the Caribbean Sea is ~0.5°C colder than the observations, but these moderate SST cold biases double to -1.1°C at LY3. Similarly, the averaged SST cold biases in MDR increases from -0.9°C at LY1 to -1.4°C at LY5. Numerous previous studies underscore its negative impacts on TC simulations (33), which can potentially constrain the HRDP's long-term prediction skills.

Nevertheless, TC empirical indices, such as MDR SST index and relative SST index (RSST; see Materials and Methods) (3), can offer some insights into HRDP's potential for longer-term TC prediction. In Table 1, the ACC values of these indices during June to November at different lead years are compared between HRDP and DPLE. The MDR index consistently demonstrates higher values in HRDP than in DPLE for all lead years. Similarly, the RSST index also exhibits higher values in HRDP compared to DPLE, except for LY1-5.

Another substantial improvement in HRDP compared to DPLE is the relationship between AMM and North Atlantic TC numbers. Notably, the correlation between AMM and TCs reaches 0.63 in HRDP (fig. S6A), indicating that ~40% of the pentadal TC number variance can be explained by AMM. Note that this high correlation between AMM and TCs in HRDP aligns with observational analysis (2), suggesting that AMM serves as valuable predictor of TCs in TNA in both HRDP and observations. In contrast, the correlation coefficient is insignificant in DPLE (0.34; fig. S6B), indicating that DPLE not only poorly simulates TCs due to its low resolution but also fails to accurately represent the observed AMM-TC relationship. This enhancement in AMM-TC relationship in HRDP highlights its potential for multiyear TC prediction in the North Atlantic.

Last, we acknowledge the complexity of the coupled prediction system and recognize that there may be additional factors contributing

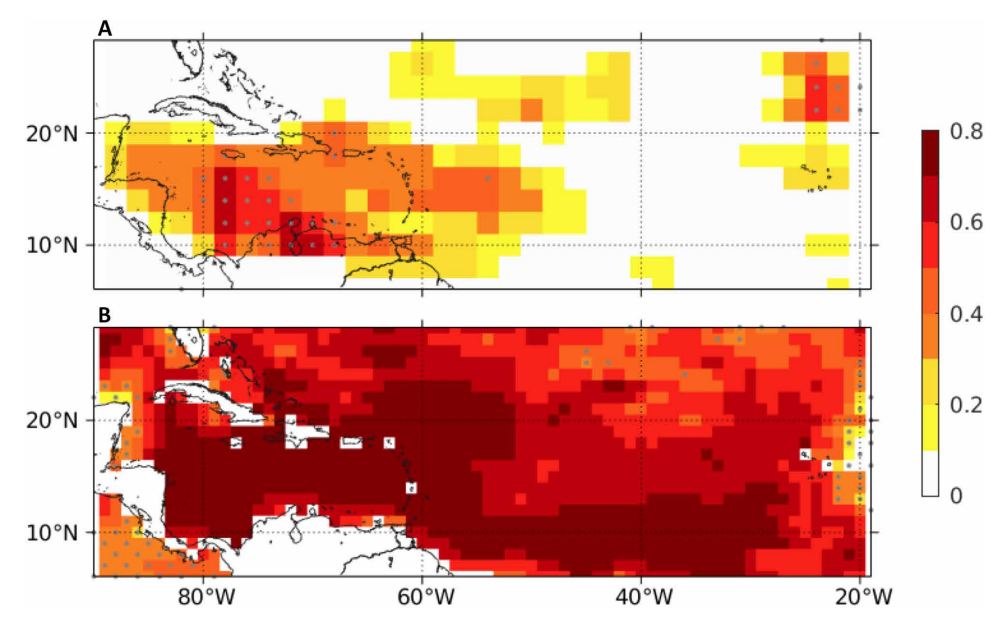


Fig. 7. HRDP prediction skill of TC track density and corresponding SST from June to November at LY1. ACC scores for (A) TC density and (B) SST. Gray dots in (A) indicate ACC skill that passes 95% significance, but in (B), those indicate ACC below 95% significant level.

Table 1. Prediction skill of TC-related SST indices from June to November. Italicized values indicate that the coefficient in HRDP is within the 0.95/0.05 quantile values of bootstrapped 10-member DPLE coefficients.

	LY1		LY1-2		LY1-3		LY1-4		LY1-5	
Index	HRDP	DPLE	HRDP	DPLE	HRDP	DPLE	HRDP	DPLE	HRDP	DPLE
MDR	0.78	0.69	0.78	0.68	0.85	0.77	0.88	0.77	0.89	0.82
RSST	0.51	0.37*	0.56	0.25*	0.55	0.34*	0.49	0.41*	0.57	0.59

^{*}The coefficient does not pass 95% significance level.

to the enhanced SST prediction that have not yet been fully accounted for. One such factor requiring careful examination in the future is the difference in ocean initial conditions between HRDP and DPLE. Preliminary analysis shows higher TNA SST ACC scores in HRDP than in DPLE at initialization (lead month 1; fig. S7, A to C). However, the ACC score of upper ocean heat content, representing ocean memory for multiyear prediction (34), only exhibits higher values than DPLE along the western boundary of the tropical Atlantic and in the northeastern TNA (fig. S7, D to F). However, over the central region of the TNA, where SST prediction is improved in HRDP, the upper ocean heat content score shows degradation compared to DPLE, raising questions about whether improved initial conditions contribute to enhanced SST prediction in TNA. This hypothesis gains further support from comparing SST ACC scores averaged over MDRs between HRDP and DPLE, where relatively minor differences are observed in LY1 and LY2 compared to LY3 to LY5 (fig. S8). In addition, remote impacts may not solely be limited to the four indices discussed in this study. Other factors with better prediction skill may also influence TNA remotely, necessitating further analysis. Moreover, quantifying the contributors to the boosted prediction skill will be the focus of future research endeavors.

In summary, the enhanced model horizontal resolution holds promising advancements in multiyear SST prediction in the TNA. This progress is linked to a more realistic portrayal of the AMM and the associated WES feedback, suggesting the potential for multiyear prediction of Atlantic TCs. Realizing this potential, however, hinges on addressing the prevalent cold SST bias in the TNA across many climate models. While flux adjustment techniques have proven effective in mitigating SST bias and achieving valuable skills in predicting TCs at seasonal timescales (35), further research is necessary to better understand the root cause of the cold bias in the TNA, enabling the reduction of its adverse impact on TC prediction within fully coupled prediction systems.

MATERIALS AND METHODS

Experimental design

All simulations are based on the CESM1. Four distinct experiment groups are considered, with each group further divided into high and low resolutions. Simulations at high horizontal resolution are based on CESM1.3 using 0.25° for atmosphere and land components coupled with 0.1° ocean and sea ice components (20). Coupled simulations at low horizontal resolution are based on CESM1.1 at nominal 1°. Uncoupled simulations at low resolution are based on CESM1.3 at nominal 1°.

Group 1: Decadal predictions

The introductions and comparisons between the CESM1 HRDP and DPLE at low resolution are described in detail by Yeager *et al.* (16). Briefly, HRDP has 10 members and 62-month integrations for each start year and is initialized from an FOSI simulation at high resolution based on the OMIP2 (19). The initial dates are every other 1 November between 1976 and 2016, that is, 21 start years. DPLE has 40 members and 122-month integrations for each start year and is initialized from an FOSI simulation at low resolution based on OMIP version 1 (OMIP1) (18). The ensemble members for both are generated by randomly perturbing the initial atmospheric temperature field at the round-off error level. The same forecast months and start years are used for comparing DPLE with HRDP.

Group 2: PI

The last 270 years of a 519-year PI-HR are used, with configuration details described by Chang *et al.* (20). In contrast, the PI-LR (21) has been integrated for 2200 years, and the period from 1900 to 2169 is extracted for comparison. Twenty independent samples including 52 model years each, avoiding the overlapping model years on purpose, are randomly selected from PI-HR and PI-LR, respectively. The purpose of the PI group is to provide a clean comparison between LR and HR that excludes the impacts of initializations and transient external forcings and only focuses on the possible differences of internal dynamical mechanisms at different resolutions.

Group 3: Uncoupled FOSI simulations

The FOSI simulations use forcing prescribed by OMIP2 at resolutions of nominal 0.1° (FOSI-HR) and 1° (FOSI-LR), respectively. They are used to investigate the sensitivity of the response of SST gradient anomalies to observation-based cross-equatorial wind anomalies at different ocean resolutions. The analysis period is between 1970 and 2016.

Group 4: Uncoupled AMIP simulations

Both AMIP-HR (three members) and AMIP-LR (five members) use a spectral element dynamical core at resolutions of 0.25° and 1°, respectively, forced by the same high-resolution (0.25°) observed SST (36). Round-off perturbations to the initial atmospheric potential temperature field are applied to generate ensembles. The analysis period is 1970–2005.

Observation validation

Prediction skill and AMM mechanism verification are relative to the following observational datasets: HadISST1 (37) and Met Office EN4.2.1 (38) for SST and upper ocean temperatures, respectively; ECMWF Reanalysis v5 (39) for wind stress and sea level pressure (SLP); the Global Precipitation Measurement (GPM) (40) for precipitation; and the international best track archive for climate stewardship dataset (41) for observed TC tracks. Only

those TCs with lifetime maximum intensity exceeding 34 knots (17.5 m/s) or higher are considered. Observations except GPM used for prediction verification are from November 1976 to December 2021 to align with HRDP and DPLE. Observed annual precipitation from GPM is used from 2001 to 2019 each other year to compare the same period of LY1-5 precipitation in HRDP and DPLE. Observations used to compare PI simulations are from January 1970 to December 2021. The observed composite of AMM events is from January 2001 to December 2021.

Prediction skill metrics

Prediction skill is evaluated by comparing observed anomalies with ensemble mean hindcast anomalies. The hindcast climatology is defined as the function of lead time. ACC is the Pearson correlation coefficient between hindcast anomalies and observational anomalies.

Forced response

The variability from forced response is defined from models in CMIP6. Considering the multimodel weighting, each model incorporates a single member serving as its representative. SST and wind stress are from 34 models, and SLP is from 35 models. Given the limited member size, traditional ensemble average may not be large enough to eliminate internal variability in particular signals related to atmosphere, such as SLP. Signal-to-noise maximizing EOF analysis (S/N), which reveals the dominant mode where all ensemble members agree on the temporal evolution (26-28, 42, 43), is used to estimate the external forcing variability. Wills et al. (26) provided detailed descriptions and codes for the S/N method. Subsequently, the forced response originating from a particular dataset is explained using a linear regression on external forcing variability derived from the multimodel S/N ensemble, following the approach outlined by Smith et al. (29). Note that we also apply two commonly used definitions of forced variability, namely, the linear trend (fig. S9, A to C) and the linear regression based on area-averaged global SST (fig. S9, D to F), to assess the sensitivity of SST ACC skill for natural variability (fig. S9). The results demonstrate the robustness of our findings shown in Fig. 1, with HRDP consistently exhibiting significantly higher ACC skill compared to DPLE when forced variability is removed.

Remote influence

The remote influence on SST in TNA is quantified through linear regression on a specific normalized index. Niño3 index is defined as the area-averaged SST anomalies in the region defined by 5°N to 5°S and 150°W to 90°W, and NAO index is defined as the SLP difference between the Azores (40°N to 34°N and 30°W to 10°W) and Iceland (68°N to 63°N and 30°W to 10°W). SEP index is the area-averaged SST anomalies within 20°S to 5°S and 120°W to 80°W. EPSO index is the area-averaged SST anomalies within 75°S to 45°S and 115°W to 70°W.

Maximum covariance analysis

MCA, which is also known as singular value decomposition, is applied to SST anomalies and combined wind stress anomalies (along-and cross-equatorial direction) in the domain 12°S to 28°N and 75°W to the African coastline. The results are consistent across various spatial extents within the tropical Atlantic. The time series from MCA are associated with the left and right singular vectors

representing the coupled variability. The spatial patterns are from the projection of normalized expansion coefficient onto the SST anomalies and wind stress anomalies, respectively, showing the structure caused by coupling. Pentadal mean in the prediction system and 3-month running mean in PI, FOSI, and AMIP are applied before analysis. In addition, both the forced response and the linear impact from remote indices (Niño3 index and NAO index) are subtracted before performing MCA analysis. Same analysis is performed to the corresponding observations. The normalization of leading MCA spatial pattern is defined as the regressed SSTAs/wind stress anomalies divided by the maximum absolute value of SSTA/ wind stress anomaly amplitude.

Composites of AMM event

AMM event is defined as the time when normalized SST expansion coefficient of MCA is larger than 1 (positive events) or lower than -1 (negative events). The AMM event composite is the difference of composites between positive and negative events. The results in PI-HR and PI-LR are derived from a 20-sample average after computing the composite of each sample. Composite normalization is defined as the AMM composite divided by the maximum absolute value from Oct0-Jul1.

TC detection, track density, MDR index, and RSST index

The HRDP-simulated TCs are detected and tracked using Tempest-Extremes algorithm (44, 45) with 6-hourly instantaneous output data. The definition of TC detection follows Roberts *et al.* (46). TC track density is defined as the total number of TCs passing through per 2° by 2° area each year, considering both TC genesis locations and the subsequent 6-hourly track paths. Following Fu *et al.* (47), the raw TC track density fields were smoothed using a nine-point moving average weighted by distance from the center of the grid box.

MDR index is the area-averaged SST over the box defined by 70°W to 20°W and 7.5°N to 22.5°N. RSST index is the difference between MDR index and the tropical mean SST² (30°S to 30°N).

Statistical analysis

The significance test for ACC is Fisher *Z*-transformation. ACC score in HRDP is considered significantly different from ACC score in DPLE when HRDP score is higher/lower than 0.95/0.05 quantile values of bootstrapped (N=500) 10-member DPLE ACC scores. In addition, ACC difference (Δ ACC) between 10-member and 40-member DPLEs (fig. S10) does not exhibit any significant distinction in SST predictions at LY1-5, in line with the results in (*16*). The median *P* value of bootstrapped (N=500) 10-member DPLE determines the significant result in fig. S8. The results from PI-HR and PI-LR are the average of 20 random samples with the same time dimension as in observations.

Supplementary Materials

This PDF file includes:

Figs. S1 to S10 Table S1

REFERENCES AND NOTES

 S. Hallam, G. D. McCarthy, X. Feng, S. A. Josey, E. Harris, A. Düsterhus, S. Ogungbenro, J. J.-M. Hirschi, The relationship between sea surface temperature anomalies, wind and translation speed and North Atlantic tropical cyclone rainfall over ocean and land. *Environ. Res. Commun.* 5, 025007 (2023).

SCIENCE ADVANCES | RESEARCH ARTICLE

- D. J. Vimont, J. P. Kossin, The Atlantic Meridional Mode and hurricane activity. Geophys. Res. Lett. 34, L07709 (2007).
- G. A. Vecchi, K. L. Swanson, B. J. Soden, Whither hurricane activity? Science 322, 687–689 (2008).
- D. J. Amaya, M. J. DeFlorio, A. J. Miller, S.-P. Xie, WES feedback and the Atlantic Meridional Mode: Observations and CMIP5 comparisons. Clim. Dyn. 49, 1665–1679 (2017).
- P. Chang, L. Ji, H. Li, A decadal climate variation in the tropical Atlantic Ocean from thermodynamic air-sea interactions. *Nature* 385, 516–518 (1997).
- J. C. H. Chiang, D. J. Vimont, Analogous Pacific and Atlantic Meridional Modes of tropical atmosphere–ocean variability. J. Clim. 17, 4143–4158 (2004).
- J. P. Kossin, D. J. Vimont, A more general framework for understanding Atlantic hurricane variability and trends. *Bull. Am. Meteorol. Soc.* 88, 1767–1782 (2007).
- 8. I. Grossmann, P. J. Klotzbach, A review of North Atlantic modes of natural variability and their driving mechanisms. *J. Geophys. Res. Atmos.* **114**, D24107 (2009).
- S.-P. Xie, S. G. H. Philander, A coupled ocean-atmosphere model of relevance to the ITCZ in the eastern Pacific. *Tellus A Dyn. Meteorol. Oceanogr.* 46, 340–350 (2022).
- D. M. Smith, R. Eade, N. J. Dunstone, D. Fereday, J. M. Murphy, H. Pohlmann, A. A. Scaife, Skilful multi-year predictions of Atlantic hurricane frequency. *Nat. Geosci.* 3, 846–849 (2010).
- A. Czaja, P. van der Vaart, J. Marshall, A diagnostic study of the role of remote forcing in tropical Atlantic variability. J. Clim. 15, 3280–3290 (2002).
- J. C. H. Chiang, Y. Kushnir, A. Giannini, Deconstructing Atlantic Intertropical Convergence Zone variability: Influence of the local cross-equatorial sea surface temperature gradient and remote forcing from the eastern equatorial Pacific. J. Geophys. Res. Atmos. 107, ACL 3-1–ACL 3-19 (2002).
- D. J. Amaya, G. R. Foltz, Impacts of canonical and Modoki El Niño on tropical Atlantic SST. J. Geophys. Res. Oceans 119, 777–789 (2014).
- N. J. Dunstone, D. M. Smith, R. Eade, Multi-year predictability of the tropical Atlantic atmosphere driven by the high latitude North Atlantic Ocean. *Geophys. Res. Lett.* 38, L14701 (2011).
- P. Chang, I. Richter, H. Dijkstra, C. Wieners, T. A. Myers, "Atmosphere-ocean interactions" in Interacting Climates of Ocean Basins Observations, Mechanisms, Predictability, and Impacts, C. R. Mechoso, Ed. (Cambridge Univ. Press, 2020), pp. 89–119; https://doi. org/10.1017/9781108610995.004.
- S. G. Yeager, P. Chang, G. Danabasoglu, N. Rosenbloom, Q. Zhang, F. S. Castruccio, A. Gopal, M. Cameron Rencurrel, I. R. Simpson, Reduced Southern Ocean warming enhances global skill and signal-to-noise in an eddy-resolving decadal prediction system. NPJ Clim. Atmos. Sci. 6, 107 (2023).
- S. G. Yeager, G. Danabasoglu, N. A. Rosenbloom, W. Strand, S. C. Bates, G. A. Meehl, A. R. Karspeck, K. Lindsay, M. C. Long, H. Teng, N. S. Lovenduski, Predicting near-term changes in the Earth system: A large ensemble of initialized decadal prediction simulations using the Community Earth System Model. *Bull. Am. Meteorol. Soc.* 99, 1867–1886 (2018).
- S. M. Griffies, G. Danabasoglu, P. J. Durack, A. J. Adcroft, V. Balaji, C. W. Böning, E. P. Chassignet, E. Curchitser, J. Deshayes, H. Drange, B. Fox-Kemper, P. J. Gleckler, J. M. Gregory, H. Haak, R. W. Hallberg, P. Heimbach, H. T. Hewitt, D. M. Holland, T. Ilyina, J. H. Jungclaus, Y. Komuro, J. P. Krasting, W. G. Large, S. J. Marsland, S. Masina, T. J. McDougall, A. J. G. Nurser, J. C. Orr, A. Pirani, F. Qiao, R. J. Stouffer, K. E. Taylor, A. M. Treguier, H. Tsujino, P. Uotila, M. Valdivieso, Q. Wang, M. Winton, S. G. Yeager, OMIP contribution to CMIP6: Experimental and diagnostic protocol for the physical component of the Ocean Model Intercomparison Project. Geosci. Model. Dev. 9, 3231–3296 (2016).
- H. Tsujino, L. S. Urakawa, S. M. Griffies, G. Danabasoglu, A. J. Adcroft, A. E. Amaral,
 T. Arsouze, M. Bentsen, R. Bernardello, C. W. Böning, A. Bozec, E. P. Chassignet, S. Danilov,
 R. Dussin, E. Exarchou, P. G. Fogli, B. Fox-Kemper, C. Guo, M. Ilicak, D. Iovino, W. M. Kim,
 N. Koldunov, V. Lapin, Y. Li, P. Lin, K. Lindsay, H. Liu, M. C. Long, Y. Komuro, S. J. Marsland,
 S. Masina, A. Nummelin, J. K. Rieck, Y. Ruprich-Robert, M. Scheinert, V. Sicardi,
 D. Sidorenko, T. Suzuki, H. Tatebe, Q. Wang, S. G. Yeager, Z. Yu, Evaluation of global
 ocean-sea-ice model simulations based on the experimental protocols of the Ocean
 Model Intercomparison Project phase 2 (OMIP-2). Geosci. Model. Dev. 13, 3643–3708
 (2020).
- P. Chang, S. Zhang, G. Danabasoglu, S. G. Yeager, H. Fu, H. Wang, F. S. Castruccio, Y. Chen, J. Edwards, D. Fu, Y. Jia, L. C. Laurindo, X. Liu, N. Rosenbloom, R. J. Small, G. Xu, Y. Zeng, Q. Zhang, J. Bacmeister, D. A. Bailey, X. Duan, A. K. DuVivier, D. Li, Y. Li, R. Neale, A. Stössel, L. Wang, Y. Zhuang, A. Baker, S. Bates, J. Dennis, X. Diao, B. Gan, A. Gopal, D. Jia, Z. Jing, X. Ma, R. Saravanan, W. G. Strand, J. Tao, H. Yang, X. Wang, Z. Wei, L. Wu, An unprecedented set of high-resolution Earth system simulations for understanding multiscale interactions in climate variability and change. *J. Adv. Model. Earth Syst.* 12, e2020MS002298 (2020).
- J. E. Kay, A. Phillips, A. Mai, C. Hannay, G. Strand, J. M. Arblaster, S. C. Bates,
 G. Danabasoglu, J. Edwards, M. Holland, P. Kushner, J.-F. Lamarque, D. Lawrence,
 K. Lindsay, A. Middleton, E. Munoz, R. Neale, K. Oleson, L. Polvani, M. Vertenstein,
 M. Vertenstein, The Community Earth System Model (CESM) large ensemble project: A

- community resource for studying climate change in the presence of internal climate variability. *Bull. Am. Meteorol. Soc.* **96**, 1333–1349 (2015).
- Y. Yang, L. Wu, Y. Guo, B. Gan, W. Cai, G. Huang, X. Li, T. Geng, Z. Jing, S. Li, X. Liang, S.-P. Xie, Greenhouse warming intensifies north tropical Atlantic climate variability. Sci. Adv. 7, eabq9690 (2021).
- C. Wang, S. Dong, Is the basin-wide warming in the North Atlantic Ocean related to atmospheric carbon dioxide and global warming? Geophys. Res Lett. 37, L08707 (2010).
- F. J. Doblas-Reyes, I. Andreu-Burillo, Y. Chikamoto, J. García-Serrano, V. Guemas, M. Kimoto, T. Mochizuki, L. R. L. Rodrigues, G. J. van Oldenborgh, Initialized near-term regional climate change prediction. *Nat. Commun.* 4, 1715 (2013).
- S. G. Yeager, J. I. Robson, Recent progress in understanding and predicting Atlantic decadal climate variability. Curr. Clim. Change Rep. 3, 112–127 (2017).
- R. C. J. Wills, D. S. Battisti, K. C. Armour, T. Schneider, C. Deser, Pattern recognition methods to separate forced responses from internal variability in climate model ensembles and observations. *J. Clim.* 33, 8693–8719 (2020).
- P. Chang, R. Saravanan, L. Ji, G. C. Hegerl, The effect of local sea surface temperatures on atmospheric circulation over the tropical Atlantic sector. J. Clim. 13, 2195–2216 (2000).
- 28. M. Ting, Y. Kushnir, R. Seager, C. Li, Forced and internal twentieth-century SST trends in the North Atlantic. *J. Clim.* **22**. 1469–1481 (2009).
- D. M. Smith, R. Eade, A. A. Scaife, L. P. Caron, G. Danabasoglu, T. M. DelSole, T. Delworth, F. J. Doblas-Reyes, N. J. Dunstone, L. Hermanson, V. Kharin, M. Kimoto, W. J. Merryfield, T. Mochizuki, W. A. Müller, H. Pohlmann, S. Yeager, X. Yang, Robust skill of decadal climate predictions. NPJ Clim. Atmos. Sci. 2. 13 (2019).
- C. M. Patricola, R. Saravanan, P. Chang, The impact of the El Niño–Southern Oscillation and Atlantic Meridional Mode on seasonal Atlantic tropical cyclone activity. J. Clim. 27, 5311–5328 (2014).
- G. R. Foltz, M. J. McPhaden, Interaction between the Atlantic Meridional and Niño Modes. Geophys. Res. Lett. 37. L18604 (2010).
- 32. A. Rugg, G. R. Foltz, R. C. Perez, Role of mixed layer dynamics in tropical North Atlantic interannual sea surface temperature variability. *J. Clim.* **29**, 8083–8101 (2016).
- W.-C. Hsu, C. M. Patricola, P. Chang, The impact of climate model sea surface temperature biases on tropical cyclone simulations. Clim. Dyn. 53, 173–192 (2019).
- S. Li, L. Zhang, L. Wu, Decadal potential predictability of upper ocean heat content over the twentieth century. Clim. Dyn. 49, 3293–3307 (2017).
- G. A. Vecchi, T. Delworth, R. Gudgel, S. Kapnick, A. Rosati, A. T. Wittenberg, F. Zeng, W. Anderson, V. Balaji, K. Dixon, L. Jia, H. S. Kim, L. Krishnamurthy, R. Msadek, W. F. Stern, S. D. Underwood, G. Villarini, X. Yang, S. Zhang, On the seasonal forecasting of regional tropical cyclone activity. *J. Clim.* 27, 7994–8016 (2014).
- R. J. Haarsma, M. J. Roberts, P. L. Vidale, C. A. Senior, A. Bellucci, Q. Bao, P. Chang, S. Corti, N. S. Fučkar, V. Guemas, J. von Hardenberg, W. Hazeleger, C. Kodama, T. Koenigk, L. R. Leung, J. Lu, J. J. Luo, J. Mao, M. S. Mizielinski, R. Mizuta, P. Nobre, M. Satoh, E. Scoccimarro, T. Semmler, J. Small, J. S. von Storch, High resolution model intercomparison project (HighResMIP v1.0) for CMIP6. Geosci. Model Dev. 9, 4185–4208 (2016).
- N. A. Rayner, D. E. Parker, E. B. Horton, C. K. Folland, L. V. Alexander, D. P. Rowell, E. C. Kent, A. Kaplan, Global analyses of sea surface temperature, sea ice, and night marine air temperature since the late nineteenth century. *J. Geophys. Res. Atmos.* 108, 2002JD002670 (2003).
- S. A. Good, M. J. Martin, N. A. Rayner, EN4: Quality controlled ocean temperature and salinity profiles and monthly objective analyses with uncertainty estimates. *J. Geophys. Res. Oceans* 118, 6704–6716 (2013).
- H. Hersbach, B. Bell, P. Berrisford, S. Hirahara, A. Horányi, J. Muñoz-Sabater, J. Nicolas, C. Peubey, R. Radu, D. Schepers, A. Simmons, C. Soci, S. Abdalla, X. Abellan, G. Balsamo, P. Bechtold, G. Biavati, J. Bidlot, M. Bonavita, G. de Chiara, P. Dahlgren, D. Dee, M. Diamantakis, R. Dragani, J. Flemming, R. Forbes, M. Fuentes, A. Geer, L. Haimberger, S. Healy, R. J. Hogan, E. Hólm, M. Janisková, S. Keeley, P. Laloyaux, P. Lopez, C. Lupu, G. Radnoti, P. de Rosnay, I. Rozum, F. Vamborg, S. Villaume, J.-N. Thépaut, The ERAS global reanalysis. Quart. J. Royal Meteoro. Soc. 146, 1999–2049 (2020).
- G. J. Huffman, E. F. Stocker, D. T. Bolvin, E. J. Nelkin, J. Tan, GPM IMERG Final Precipitation L3
 1 Day 0.1 Degree x 0.1 Degree V06, (NASA Goddard Earth Sciences Data and Information Services Center. 2019): https://doi.org/10.5067/GPM/IMERGDF/DAY/06.
- K. R. Knapp, M. C. Kruk, D. H. Levinson, H. J. Diamond, C. J. Neumann, The international best track archive for climate stewardship (IBTrACS). *Bull. Am. Meteorol. Soc.* 91, 363–376 (2010)
- S. Venzke, M. R. Allen, R. T. Sutton, D. P. Rowell, The atmospheric response over the North Atlantic to decadal changes in sea surface temperature. J. Clim. 12, 2562–2584 (1999).
- M. R. Allen, L. A. Smith, Optimal filtering in singular spectrum analysis. *Phys. Lett. A* 234, 419–428 (1997).
- C. M. Zarzycki, P. A. Ullrich, Assessing sensitivities in algorithmic detection of tropical cyclones in climate data. Geophys. Res. Lett. 44, 1141–1149 (2017).
- P. A. Ullrich, C. M. Zarzycki, TempestExtremes: A framework for scale-insensitive pointwise feature tracking on unstructured grids. Geosci. Model Dev. 10, 1069–1090 (2017).

SCIENCE ADVANCES | RESEARCH ARTICLE

- M. J. Roberts, J. Camp, J. Seddon, P. L. Vidale, K. Hodges, B. Vannière, J. Mecking, R. Haarsma, A. Bellucci, E. Scoccimarro, L. P. Caron, F. Chauvin, L. Terray, S. Valcke, M. P. Moine, D. Putrasahan, C. D. Roberts, R. Senan, C. Zarzycki, P. Ullrich, Y. Yamada, R. Mizuta, C. Kodama, D. Fu, Q. Zhang, G. Danabasoglu, N. Rosenbloom, H. Wang, L. Wu, Projected future changes in tropical cyclones using the CMIP6 HighResMIP multimodel ensemble. Geophys. Res. Lett. 47, e2020GL088662 (2020).
- D. Fu, P. Chang, C. M. Patricola, Intrabasin variability of East Pacific tropical cyclones during ENSO regulated by Central American Gap Winds. Sci. Rep. 7, 1658 (2017).

Acknowledgments: The HRDP experiments were performed by the International Laboratory for High-Resolution Earth System Predictions (iHESP). Q.Z. acknowledges the support from the China Scholarship Council. We thank TAMU Supercomputing Facility and the Texas Advanced Computing Center (TACC) for providing the computing resources for this research. Funding: This research is partially supported by the grants as follows: U.S. National Science Foundation (NSF) grant AGS-2231237; the Gulf Research Program of the U.S. National Academies of Sciences, Engineering, and Medicine 2000013283; and the Department of Commerce through the Climate Variability and Predictability Program of NOAA OAR's Climate Program Office NA20OAR4310408. The CESM project is supported primarily by the U.S. NSF. The NSF NCAR is a major facility sponsored by the U.S. NSF under cooperative agreement 1852977. Author contributions: Conceptualization: Q.Z. and P.C. Model simulation: Q.Z., F.C.,

and N.R. Investigation: Q.Z., P.C., D.F., S.G.Y., and G.D. Analysis and figures: Q.Z., P.C., and D.F. Supervision: P.C., S.G.Y., and G.D. Writing—original draft: Q.Z., P.C., and D.F. Writing—review and editing: Q.Z., P.C., D.F., S.G.Y., and G.D. Competing interests: The authors declare that they have no competing interests. Data and materials availability: All data needed to evaluate the conclusions in the paper are present in the paper and/or the Supplementary Materials. The processed data from HRDP, FOSI-HR, FOSI-LR, AMIP-HR, and AMIP-LR used in this paper are available at https://dataverse.tdl.org/dataverse/enhanced_amm. DPLE is available at www.earthsystemgrid.org/dataset/ucar.cgd.ccsm4.CESM1-CAM5-DP.html. Models from CMIP6 are downloaded from https://cds.climate.copernicus.eu/cdsapp#l/dataset/projections-cmip6?tab=overview. The PI-HR is available at https://ihesp.github.io/archive/products/ihesp-products/data-release/DataRelease_Phase2.html. PI-LR can be reached at different ways with the information at www.cesm.ucar.edu/community-projects/lens/data-sets. DPLE and PI-LR are generated by the CESM1.1 code, which is available at www.cesm.ucar.edu/models/cesm1.1/index.html. Other simulations used in this manuscript are generated by the CESM1.3 code available https://zenodo.org/records/10888306.

Submitted 12 February 2024 Accepted 27 June 2024 Published 2 August 2024 10.1126/sciadv.ado6298